Electronics and Electrical Engineering

AIMS Electronics and Electrical Engineering, 9(3): 288–313.
DOI: 10.3934/electreng.2025014
Received: 23 December 2024
Revised: 10 May 2025
Accepted: 22 May 2025
Published: 05 June 2025

http://www.aimspress.com/journal/ElectrEng

Research article

Comprehensive GSSA and D-Q frame dynamic modeling of dual-active-bridge DC-DC converters

José M. Campos-Salazar[1,*], Roya Rafiezadeh[2], Felipe Santander[3], Juan L. Aguayo-Lazcano[4] and Nicolás Kunakov[5]

[1] Electronic Engineering Department, Universitat Politècnica de Catalunya, Barcelona, Spain
[2] Power Electronics and Machine Centre, University of Nottingham, Nottingham, United Kingdom
[3] Process Control Department, Celulosa Arauco y Constitución S.A, Concepción, Chile
[4] Institute of Physical and Mathematical Sciences, Universidad Austral de Chile, Valdivia, Chile
[5] Reliability Department, Celulosa Arauco y Constitución S.A, Valdivia, Chile

* **Correspondence:** Email: jose.campos.salazar@upc.edu.

Abstract: Dynamic modeling and control of DC–DC power converters require formulations capable of capturing nonlinearity, harmonic interaction, and control sensitivity under fast-switching and bidirectional power flow. The two-level dual-active-bridge (2L-DAB) converter exemplifies such challenges, especially under phase-shift modulation schemes used for galvanically isolated energy transfer. To address these issues, three complementary modeling frameworks are developed: a switching model in the time domain, a rotating-frame formulation based on the DQ transformation, and a generalized state-space averaging (GSSA) model that incorporates fundamental and harmonic components through frequency-domain decomposition. Each formulation enables a different perspective—ranging from intuitive time-domain dynamics to harmonic coupling behavior—while providing a foundation for control system design. Small-signal linearizations yield control-to-output transfer functions used for loop-shaping via proportional-integral (PI) compensators. A modified phase margin criterion is employed to guarantee dynamic stability and robustness. Comparative simulation results under reference and load disturbances demonstrate the distinct advantages of each model, with the GSSA approach excelling in harmonic accuracy and the DQ-based model offering streamlined controller implementation. These tools offer a robust methodology for high-fidelity analysis and design of high-performance DAB-based systems.

Keywords: control strategy; D-Q modeling; dual-active-bridge converter; generalized state-space

averaging; power electronics; simulation

1. Introduction

The dual active bridge (DAB) DC–DC converter has established itself as a pivotal topology for galvanically isolated, high-efficiency, bidirectional power transfer, with widespread applicability across electric vehicles, energy storage systems, solid-state transformers, and renewable energy integration frameworks [1–3]. Its architectural symmetry, inherent soft-switching properties, and modular high-power scalability have led to intensive academic and industrial focus over the past two decades. The fundamental understanding of DAB operation has evolved through various modeling and control approaches—ranging from piecewise analytical solutions and energy balance equations [4,5] to reduced-order averaged models [6,7] and control-oriented state-space formulations [8,9]. Early contributions centered on steady-state power flow derivations and zero-voltage-switching boundary conditions [6,10], setting the stage for systematic exploration into dynamic behavior and control mechanisms. In this context, generalized average modeling and generalized state-space averaging (GSSA) have emerged as powerful tools for extending classical averaging into the harmonic domain, enabling Fourier-based characterization of high-frequency AC-link variables [7,11,12].

Recent developments in GSSA formulations highlight its capability to capture both large- and small-signal dynamics of DAB converters under various modulation schemes, including single-phase shift, dual-phase shift, and triple-phase shift strategies [7,13]. Compared to conventional state-space averaging—which fails to represent high-frequency harmonic content in switching converters—the GSSA method leverages sliding-window Fourier decomposition to construct frequency-domain models where each coefficient represents a specific harmonic order [7,11,12]. Enhanced models further incorporate third- and higher-order harmonics for improved accuracy under light-load or dynamic conditions, particularly addressing losses due to conduction and core effects [14]. Moreover, several recent works have introduced flexible harmonic-domain and linear time-periodic methods to selectively include relevant harmonics per state variable, balancing modeling complexity and fidelity [15,16].

In parallel, modeling approaches based on the DQ transformation have offered alternative insights by translating AC variables into quasi-stationary rotating reference frames, suitable for identifying control interactions and dynamic coupling in dual-active systems [17–19]. These DQ-domain averaged models, while powerful in simplifying modulator-frame dynamics, often require specific assumptions on signal periodicity and symmetry and may obscure harmonic-rich interactions unless explicitly extended. Therefore, comparing DQ-based and GSSA-based models offers valuable perspectives on modeling scope, frequency content, and simulation tradeoffs, particularly in control design, loop gain analysis, and harmonic sensitivity evaluation. This article aims to develop, analyze, and compare large-signal averaged models for the DAB converter using both the DQ transformation and the GSSA framework, integrating harmonic decomposition, Fourier-based averaging, and control-oriented dynamic modeling. To this end, this work presents a unified modeling framework for the two-level DAB converter.

First, the large-signal time-domain model is derived and analyzed to identify switching dynamics. Then, two distinct averaged modeling strategies are applied: the DQ-coordinate-based model and the GSSA model. These are mathematically developed and validated, with comparative analysis conducted on dynamic response and structural complexity. Moreover, the article explores

implications for small-signal linearization, PI control design, and loop gain-based stability analysis. Simulation results validate the accuracy and robustness of each approach under typical and disturbed operation scenarios.

The manuscript is organized as follows: Section 2 introduces the dual-active-bridge converter topology, detailing its main components and operating principles. Section 3 develops the system-level modeling of the converter, including switching models, large-signal averaged representations, and coordinate-transformed frameworks. Section 4 presents the design and implementation of the control system, emphasizing PI compensator synthesis, loop gain tuning, and frequency-domain stability analysis. Section 5 provides a sensitivity analysis to evaluate the influence of key parameters on dynamic performance. Section 6 reports simulation results under various operating scenarios, validating both the control design and theoretical models. Finally, Section 7 concludes the paper by summarizing the main contributions and outlining perspectives for future work.

2. Dual-active-bridge converter topology

The 2L-DAB converter topology (Figure 1) includes four main stages: A- and B-side DC links, full-bridge (FB) switching networks on each side, a load resistor, and an high-frequency transformer (HFT) enabling bidirectional power flow. Dynamic variables comprise input voltage and current $v_i(t)$ and $i_i(t)$; currents $i_{2A}(t)$ and $i_{2B}(t)$ entering the A- and B-side switching networks, respectively; voltages and currents across capacitors $v_{CA}(t)$, $v_{CB}(t)$, $i_{CA}(t)$, and $i_{CB}(t)$; and HFT terminal voltages and currents $v_a(t)$, $v_b(t)$, $i_a(t)$, and $i_b(t)$. The output voltage is given by $v_L(t) = v_{CB}(t)$. Parameters include source resistance R_i, DC-link capacitors C_A and C_B, load resistance R_L, and HFT leakage inductance and resistance L_k and r_{Lk}, respectively. Also, n is the number of turns of the primary winding. Finally, each FB consists of two switching legs with switches Q_{xA} on the A side and Q_{xB} on the B side for $x \in \{1, 2, 3, 4\}$.

3. System modeling

This section develops the 2L-DAB converter's mathematical models in switching, large-signal, and small-signal versions.

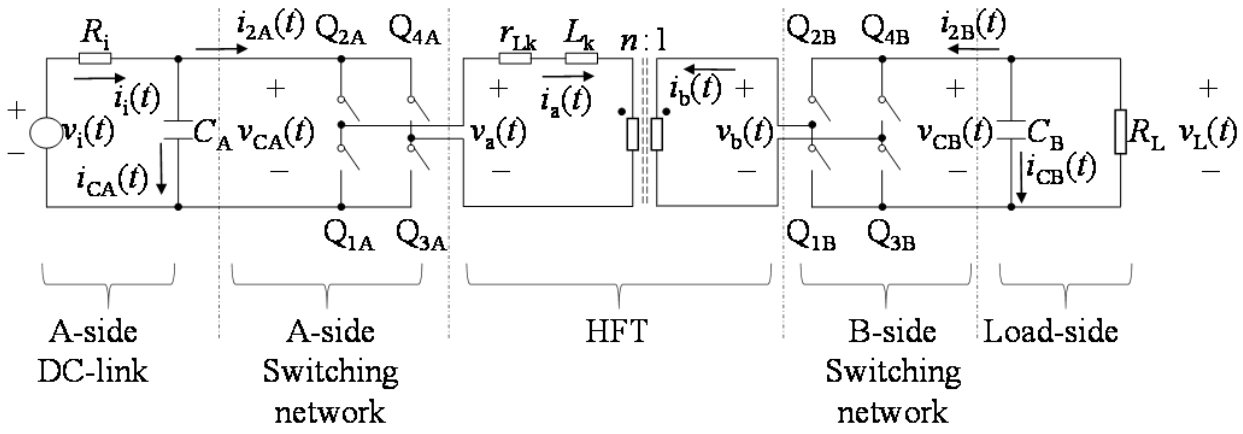

Figure 1. 2L-DAB converter topology.

3.1. Switching model

This model is derived from the switching representation in Figure 1. The converter's structure allows for separate stage modeling while maintaining consistent voltage and current references [13]. The A-side DC-link dynamic model is thus defined as:

$$\frac{\mathrm{d}v_{\mathrm{CA}}(t)}{\mathrm{d}t} = -\frac{1}{\tau_{\mathrm{A}}}\cdot v_{\mathrm{CA}}(t) + \frac{1}{\tau_{\mathrm{A}}}\cdot v_{\mathrm{CA}}(t) - \frac{R_{\mathrm{i}}}{\tau_{\mathrm{A}}}\cdot i_{2\mathrm{A}}(t) \tag{1}$$

where $\tau_{\mathrm{A}} = R_{\mathrm{i}}\cdot C_{\mathrm{A}}$ is the A-side time constant in seconds (s).

The load-side dynamical equation can be defined as:

$$\frac{\mathrm{d}v_{\mathrm{CB}}(t)}{\mathrm{d}t} = -\frac{1}{\tau_{\mathrm{B}}}\cdot v_{\mathrm{CB}}(t) - \frac{R_{\mathrm{L}}}{\tau_{\mathrm{B}}}\cdot i_{2\mathrm{B}}(t) \tag{2}$$

where $\tau_{\mathrm{B}} = R_{\mathrm{L}}\cdot C_{\mathrm{B}}$ is the B-side (load-side) time constant in s.

The dynamic model of the HFT is defined as:

$$\frac{\mathrm{d}i_{\mathrm{a}}(t)}{\mathrm{d}t} = -\frac{1}{\tau_{\mathrm{HFT}}}\cdot i_{\mathrm{a}}(t) + \frac{r_{\mathrm{Lk}}}{\tau_{\mathrm{HFT}}}\cdot v_{\mathrm{a}}(t) - \frac{n\cdot r_{\mathrm{Lk}}}{\tau_{\mathrm{HFT}}}\cdot v_{\mathrm{b}}(t) \tag{3}$$

Also, $\tau_{\mathrm{HFT}} = L_{\mathrm{k}}/r_{\mathrm{Lk}}$ is the HFT time constant in s.

Modeling the switching networks requires representing the switching strategies for each FB structure, as shown in Figure 2. The switching function for the A-side FB, $s_{\mathrm{A}}(t)$, is depicted in Figure 2(a), where designator 1 indicates that switches $Q_{2\mathrm{A}}$ and $Q_{3\mathrm{A}}$ are active, while $Q_{1\mathrm{A}}$ and $Q_{4\mathrm{A}}$ are inactive. In designator 2, the states are reversed. Figure 2(b) illustrates the B-side FB switching function $s_{\mathrm{B}}(t)$, in which designators 1 and 3 indicate that $Q_{1\mathrm{B}}$ and $Q_{4\mathrm{B}}$ are active while $Q_{2\mathrm{B}}$ and $Q_{3\mathrm{B}}$ are inactive. Designator 2 implies the inverted states. The switching function $s_X(t)$ ($X \in \{\mathrm{A}, \mathrm{B}\}$) is defined as follows [13,20,21]:

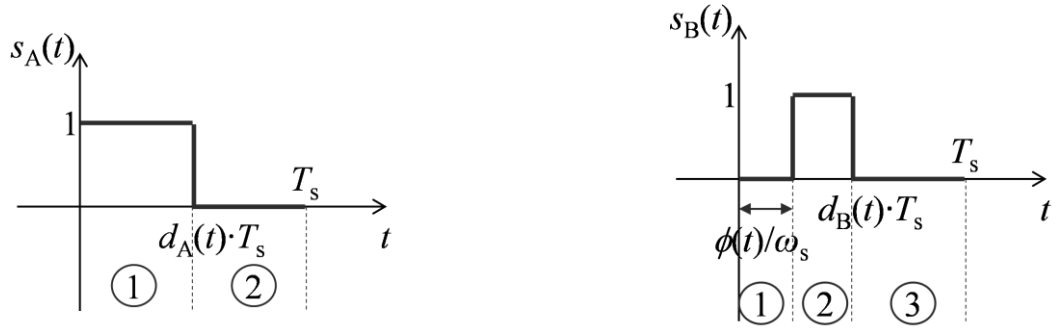

(a) (b)

Figure 2. Definition of the switching functions associated with the FBs of the A and B sides. (a) $s_{\mathrm{A}}(t)$. (b) $s_{\mathrm{B}}(t)$.

$$\begin{cases} s_{\mathrm{A}}(t) = \begin{cases} 1, & 0 \le t < \dfrac{1}{2}\cdot d_{\mathrm{A}}(t)\cdot T_{\mathrm{s}} \\ 0, & \dfrac{1}{2}\cdot d_{\mathrm{A}}(t)\cdot T_{\mathrm{s}} \le t < T_{\mathrm{s}} \end{cases} \\ s_{\mathrm{B}}(t) = \begin{cases} 1, & \dfrac{1}{2}\cdot d_{\mathrm{B}}(t)\cdot T_{\mathrm{s}} \le t < \dfrac{1}{2}\cdot T_{\mathrm{s}} + \dfrac{1}{2}\cdot d_{\mathrm{B}}(t)\cdot T_{\mathrm{s}} \\ 0, & \dfrac{1}{2}\cdot T_{\mathrm{s}} + \dfrac{1}{2}\cdot d_{\mathrm{B}}(t)\cdot T_{\mathrm{s}} \le t < T_{\mathrm{s}} \end{cases} \end{cases} \tag{4}$$

where $s_X(t)$ (for $X \in \{\mathrm{A}, \mathrm{B}\}$) are phase-shifted by $\phi(t)$ [1]. From here, T_{s} represents the switching period, and $d_X(t)$ denotes the duty cycle over T_{s} associated with the operation of both FBs.

Applying Kirchhoff's voltage and current laws to the switching networks on both sides of the converter, as shown in Figure 1, yields relationships between the DC links and the HFT terminal ports. Consequently, the voltage and current expressions for both sides of the converter are defined as follows:

$$\begin{bmatrix} v_x(t) \\ i_{2X}(t) \end{bmatrix} = 2\cdot(\mathrm{s_X}(t) - 1/2)\cdot \mathbf{I}_2 \cdot \begin{bmatrix} v_{CX}(t) \\ i_x(t) \end{bmatrix} \tag{5}$$

From here, $x \in \{\mathrm{a}, \mathrm{b}\}$, $X \in \{\mathrm{A}, \mathrm{B}\}$, and $\mathbf{I}_2$ is the identity matrix of size 2. From (1)–(5), the dynamic switching model can be defined as follows:

$$\begin{cases} \mathrm{d}v_{\mathrm{CA}}(t)/\mathrm{d}t = (1/\tau_{\mathrm{A}})\cdot\left(-v_{\mathrm{CA}}(t) + v_{\mathrm{i}}(t) - 2\cdot R_{\mathrm{i}}\cdot(s_{\mathrm{A}}(t) - 1/2)\cdot i_{\mathrm{a}}(t)\right) \\ \mathrm{d}i_{\mathrm{a}}(t)/\mathrm{d}t = (1/\tau_{\mathrm{HFT}})\cdot\left(-i_{\mathrm{a}}(t) + 2\cdot r_{\mathrm{Lk}}\cdot(s_{\mathrm{A}}(\mathrm{t}) - 1/2)\cdot v_{\mathrm{CA}}(t) - 2\cdot r_{\mathrm{Lk}}\cdot(s_{\mathrm{B}}(t) - 1/2)\cdot v_{\mathrm{CB}}(t)\right. \\ \mathrm{d}v_{\mathrm{CB}}(\mathrm{t})/\mathrm{d}t = (1/\tau_{\mathrm{B}})\cdot\left(-v_{\mathrm{CB}}(t) - 2\cdot n\cdot R_{\mathrm{L}}\cdot(s_{\mathrm{B}}(t) - 1/2)\cdot i_{\mathrm{a}}(t)\right) \end{cases} \tag{6}$$

From (6), it is evident that the system's dynamic behavior is discrete due to the switching functions $s_{\mathrm{A}}(t)$ and $s_{\mathrm{B}}(t)$, introducing a high degree of nonlinearity.

3.2. Large-signal averaged model and comparative framework

The switching model presented in (6) serves as a foundational framework for implementing nonlinear control strategies such as hysteresis-based schemes, boundary control, and sliding-mode regulators [13,20]. Despite its precision in characterizing the instantaneous switching behavior of the DAB converter, its discontinuous nature complicates control-oriented analysis in the frequency domain, especially when dynamic phasor or DQ-based transformations are required.

To facilitate the transition toward a tractable linear model in the D-Q rotating reference frame, a continuous-time averaged representation is first derived. This intermediate model bridges the gap between the time-domain switching behavior and the desired frequency-domain analytical formulations. By applying the classical time-averaging operator over one switching period T_{s}, in the spirit of state-space averaging theory [22], the large-signal averaged model is obtained as follows:

$$\begin{cases} \mathrm{d}\langle v_{\mathrm{CA}}(t)\rangle_{T_\mathrm{s}}/\mathrm{d}t = (1/\tau_\mathrm{A})\cdot\left(-\langle v_{\mathrm{CA}}(t)\rangle_{T_\mathrm{s}} + \langle v_\mathrm{i}(t)\rangle_{T_\mathrm{s}} - 2\cdot R_\mathrm{i}\cdot(d_\mathrm{A}(t)-1/2)\cdot\langle i_\mathrm{a}(t)\rangle_{T_\mathrm{s}}\right) \\ \mathrm{d}\langle i_\mathrm{a}(t)\rangle_{T_\mathrm{s}}/\mathrm{d}t = (1/\tau_{\mathrm{HFT}})\cdot\left(-\langle i_\mathrm{a}(t)\rangle_{T_\mathrm{s}} + 2\cdot r_{\mathrm{Lk}}\cdot(d_\mathrm{A}(t)-1/2)\cdot\langle v_{\mathrm{CA}}(t)\rangle_{T_\mathrm{s}} - \right. \\ \left. -2\cdot r_{\mathrm{Lk}}\cdot(d_\mathrm{B}(t)-1/2)\cdot\langle v_{\mathrm{CB}}(t)\rangle_{T_\mathrm{s}}\right) \\ \mathrm{d}\langle v_{\mathrm{CB}}(t)\rangle_{T_\mathrm{s}}/\mathrm{d}t = (1/\tau_\mathrm{B})\cdot\left(-\langle v_{\mathrm{CB}}(t)\rangle_{T_\mathrm{s}} - 2\cdot n\cdot R_\mathrm{L}\cdot(d_\mathrm{B}(t)-1/2)\cdot\langle i_\mathrm{a}(t)\rangle_{T_\mathrm{s}}\right) \end{cases} \tag{7}$$

Here, $d_X(t) = \langle s_X(t)\rangle_{T\mathrm{s}}$ approximates the averaged switching function for bridge $X \in \{\mathrm{A}, \mathrm{B}\}$, and $\tau_\mathrm{A} = R_\mathrm{i}\cdot C_\mathrm{A}$, $\tau_\mathrm{B} = R_\mathrm{L}\cdot C_\mathrm{B}$, $\tau_{\mathrm{HFT}} = r_{\mathrm{Lk}}/L_\mathrm{k}$ are the associated time constants.

Although (7) provides a continuous representation suitable for controller synthesis, it remains inherently nonlinear due to the multiplicative terms involving $d_X(t)$ and the state variables. To circumvent this, and to decouple HFT dynamics from the rest of the system, a transformation into the rotating D-Q reference frame is adopted [23]. This transformation linearizes the sinusoidal dynamics of the HFT and enables explicit separation of active and reactive power contributions in the averaged model.

By applying the Park transformation and assuming sinusoidal steady-state behavior at the HFT terminals, the D-Q frame model of the HFT is obtained as follows:

$$\begin{cases} \dfrac{\mathrm{d}\langle i_\mathrm{a}^\mathrm{d}(t)\rangle_{T_\mathrm{s}}}{\mathrm{d}t} = \dfrac{1}{\tau_{\mathrm{HFT}}}\cdot\left(-\langle i_\mathrm{a}^\mathrm{d}(t)\rangle_{T_\mathrm{s}} + \omega_\mathrm{s}\cdot\tau_{\mathrm{HFT}}\cdot\langle i_\mathrm{a}^\mathrm{q}(t)\rangle_{T_\mathrm{s}} + r_{\mathrm{Lk}}\cdot\langle v_\mathrm{a}^\mathrm{d}(t)\rangle_{T_\mathrm{s}} - n\cdot r_{\mathrm{Lk}}\cdot\langle v_\mathrm{b}^\mathrm{d}(t)\rangle_{T_\mathrm{s}}\right) \\ \dfrac{\mathrm{d}\langle i_\mathrm{a}^\mathrm{q}(t)\rangle_{T_\mathrm{s}}}{\mathrm{d}t} = \dfrac{1}{\tau_{\mathrm{HFT}}}\cdot\left(-\langle i_\mathrm{a}^\mathrm{q}(t)\rangle_{T_\mathrm{s}} - \omega_\mathrm{s}\cdot\tau_{\mathrm{HFT}}\cdot\langle i_\mathrm{a}^\mathrm{d}(t)\rangle_{T_\mathrm{s}} + r_{\mathrm{Lk}}\cdot\langle v_\mathrm{a}^\mathrm{q}(t)\rangle_{T_\mathrm{s}} - n\cdot r_{\mathrm{Lk}}\cdot\langle v_\mathrm{b}^\mathrm{q}(t)\rangle_{T_\mathrm{s}}\right) \end{cases} \tag{8}$$

To remove switching functions entirely, power conservation is imposed on both sides of the HFT. By equating the instantaneous D-Q frame power between the HFT and the respective DC-links, the average output and input currents are expressed as functions of the D-Q terminal voltages and currents, as follows:

$$\begin{cases} \langle i_{2\mathrm{A}}(t)\rangle_{T_\mathrm{s}} = -\left[\dfrac{\langle v_\mathrm{a}^\mathrm{d}(t)\rangle_{T_\mathrm{s}}\cdot\langle i_\mathrm{a}^\mathrm{d}(t)\rangle_{T_\mathrm{s}}}{\langle v_{\mathrm{CA}}(t)\rangle_{T_\mathrm{s}}} + \dfrac{\langle v_\mathrm{a}^\mathrm{q}(t)\rangle_{T_\mathrm{s}}\cdot\langle i_\mathrm{a}^\mathrm{q}(t)\rangle_{T_\mathrm{s}}}{\langle v_{\mathrm{CA}}(t)\rangle_{T_\mathrm{s}}}\right] \\ \langle i_{2\mathrm{B}}(t)\rangle_{T_\mathrm{s}} = -n\cdot\left[\dfrac{\langle v_\mathrm{b}^\mathrm{d}(t)\rangle_{T_\mathrm{s}}\cdot\langle i_\mathrm{a}^\mathrm{d}(t)\rangle_{T_\mathrm{s}}}{\langle v_{\mathrm{CB}}(t)\rangle_{T_\mathrm{s}}} + \dfrac{\langle v_\mathrm{b}^\mathrm{q}(t)\rangle_{T_\mathrm{s}}\cdot\langle i_\mathrm{a}^\mathrm{q}(t)\rangle_{T_\mathrm{s}}}{\langle v_{\mathrm{CB}}(t)\rangle_{T_\mathrm{s}}}\right] \end{cases} \tag{9}$$

By substituting (9) into the capacitor current balance equations and combining with the D-Q model in (8), the complete large-signal averaged model of the 2L-DAB converter in the rotating D-Q frame is derived as follows:

$$
\begin{cases}
\mathrm{d}\langle v_{\mathrm{CA}}(t)\rangle_{T_s}/\mathrm{d}t = (1/\tau_{\mathrm{A}})\cdot\Big(-\langle v_{\mathrm{CA}}(t)\rangle_{T_s} + \langle v_{\mathrm{i}}(t)\rangle_{T_s} - \\
\qquad -R_{\mathrm{i}}\cdot\left(\dfrac{\langle v_{\mathrm{a}}^{\mathrm{d}}(t)\rangle_{T_s}\cdot\langle i_{\mathrm{a}}^{\mathrm{d}}(t)\rangle_{T_s} + \langle v_{\mathrm{a}}^{\mathrm{q}}(t)\rangle_{T_s}\cdot\langle i_{\mathrm{a}}^{\mathrm{q}}(t)\rangle_{T_s}}{\langle v_{\mathrm{CA}}(t)\rangle_{T_s}}\right)\Big) \\
\mathrm{d}\langle i_{\mathrm{a}}^{\mathrm{d}}(t)\rangle_{T_s}/\mathrm{d}t = (1/\tau_{\mathrm{HFT}})\cdot\Big(-\langle i_{\mathrm{a}}^{\mathrm{d}}(t)\rangle_{T_s} + \omega_{\mathrm{s}}\cdot\tau_{\mathrm{HFT}}\cdot\langle i_{\mathrm{a}}^{\mathrm{q}}(t)\rangle_{T_s} + r_{\mathrm{Lk}}\cdot\langle v_{\mathrm{a}}^{\mathrm{d}}(t)\rangle_{T_s} - n\cdot r_{\mathrm{Lk}}\cdot\langle v_{\mathrm{b}}^{\mathrm{d}}(t)\rangle_{T_s}\Big) \\
\mathrm{d}\langle i_{\mathrm{a}}^{\mathrm{q}}(t)\rangle_{T_s}/\mathrm{d}t = (1/\tau_{\mathrm{HFT}})\cdot\Big(-\langle i_{\mathrm{a}}^{\mathrm{q}}(t)\rangle_{T_s} - \omega_{\mathrm{s}}\cdot\tau_{\mathrm{HFT}}\cdot\langle i_{\mathrm{a}}^{\mathrm{d}}(t)\rangle_{T_s} + r_{\mathrm{Lk}}\cdot\langle v_{\mathrm{a}}^{\mathrm{q}}(t)\rangle_{T_s} - n\cdot r_{\mathrm{Lk}}\cdot\langle v_{\mathrm{b}}^{\mathrm{q}}(t)\rangle_{T_s}\Big) \\
\mathrm{d}\langle v_{\mathrm{CB}}(t)\rangle_{T_s}/\mathrm{d}t = (1/\tau_{\mathrm{B}})\cdot\Big(-\langle v_{\mathrm{CB}}(t)\rangle_{T_s} - \\
\qquad -n\cdot R_{\mathrm{L}}\cdot\left(\dfrac{\langle v_{\mathrm{b}}^{\mathrm{d}}(t)\rangle_{T_s}\cdot\langle i_{\mathrm{a}}^{\mathrm{d}}(t)\rangle_{T_s} + \langle v_{\mathrm{b}}^{\mathrm{q}}(t)\rangle_{T_s}\cdot\langle i_{\mathrm{a}}^{\mathrm{q}}(t)\rangle_{T_s}}{\langle v_{\mathrm{CB}}(t)\rangle_{T_s}}\right)\Big)
\end{cases}
\tag{10}
$$

This model forms the core of the frequency-domain representation of the converter and reveals the coupling between the active (D) and reactive (Q) components of the HFT terminal variables.

Figure 3 graphically illustrates the electrical interpretation of model (10). The circuit comprises four interconnected subcircuits: two voltage-source networks modeling the HFT D-Q dynamics and two current-source networks capturing the input and output DC-link energy transfer. The voltage-source channels feature controlled excitations at both input and output terminals that reflect the cross-link interaction via X_{Lk} and n. Meanwhile, the current-source subcircuits inject averaged powers P_{adq} and P_{bdq}, derived as inner products of voltage and current components in the D-Q frame.

This modular configuration enables intuitive interpretation of dynamic power flow and average voltage regulation under transient scenarios. Unlike traditional time-domain approaches, the D-Q model isolates system modes by exploiting orthogonal components aligned with rotating phasors, simplifying linear control synthesis.

To rigorously characterize the dynamic behavior of the model in (10), it is instructive to compare it against a model derived through the GSSA method—a well-established technique with strong theoretical foundations and validated applications in power electronics modeling [11,24,25]. Unlike classical averaging or DQ-based formulations, the GSSA framework provides a natural representation of multifrequency behavior in converters operating under periodic steady-state conditions, making it particularly suitable for converters such as the 2L-DAB, whose AC-port variables inherently oscillate at high switching frequencies.

The formulation begins by considering the original switching model in (6), which incorporates the piecewise switching functions $s_X(t)$ (with $X \in \{\mathrm{A}, \mathrm{B}\}$) modulating the bridge operation. For tractability, and in line with standard practice in generalized averaging [24,25], the substitution $2\cdot(s_X(t)-0.5) \approx s_X(t)$ is introduced. This approximation linearizes the switching action around its nominal duty-cycle midpoint and simplifies the harmonic decomposition.

Applying the GSSA operator, which projects periodic signals into their DC and fundamental harmonic components, to the system in (6) and isolating the relevant dynamic harmonics (zeroth and first), the following coupled system is derived as follows:

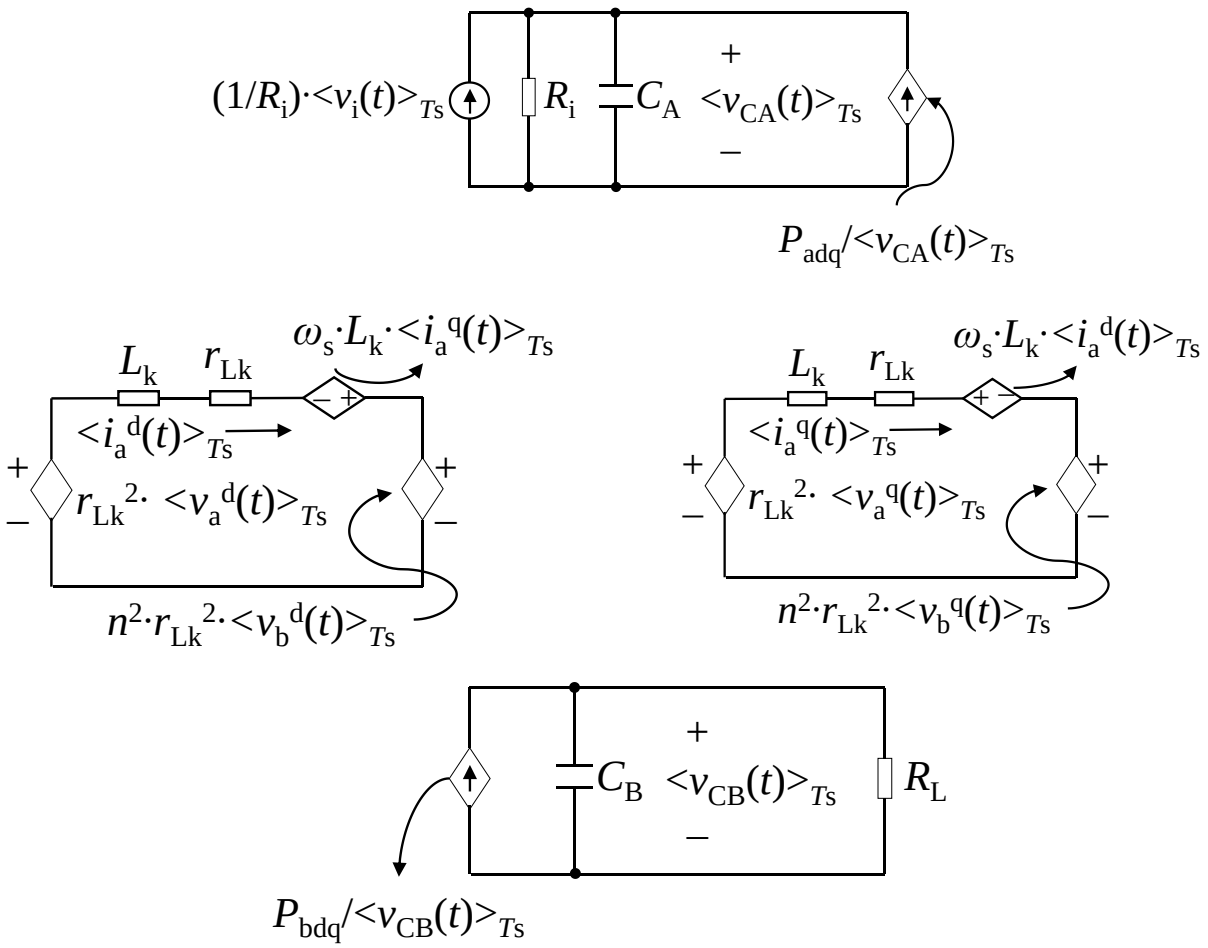

Figure 3. 2L-DAB averaged model in DQ coordinates. Model built with two voltage source circuits (that model the transformer) and two current source circuits (that generate the interaction between the system power supply and its output).

$$\begin{cases} \dfrac{\mathrm{d}\langle v_{\mathrm{CA}}\rangle_0}{\mathrm{d}t} \approx \dfrac{1}{\tau_{\mathrm{A}}}\cdot(-\langle v_{\mathrm{CA}}\rangle_0 + \langle v_{\mathrm{i}}\rangle_0 - R_{\mathrm{i}}\cdot\langle s_{\mathrm{A}}\cdot i_{\mathrm{a}}\rangle_0) \\ \dfrac{\mathrm{d}\langle i_{\mathrm{a}}\rangle_1}{\mathrm{d}t} \approx \dfrac{1}{\tau_{\mathrm{HFT}}}\cdot(-\langle i_{\mathrm{a}}\rangle_1 + r_{\mathrm{Lk}}\cdot\langle s_{\mathrm{A}}\cdot v_{\mathrm{CA}}\rangle_1 - r_{\mathrm{Lk}}\cdot\langle s_{\mathrm{B}}\cdot v_{\mathrm{CB}}\rangle_1) \\ \dfrac{\mathrm{d}\langle v_{\mathrm{CB}}\rangle_0}{\mathrm{d}t} \approx \dfrac{1}{\tau_{\mathrm{B}}}\cdot(-\langle v_{\mathrm{CB}}\rangle_0 - n\cdot R_{\mathrm{L}}\cdot\langle s_{\mathrm{B}}\cdot i_{\mathrm{a}}\rangle_0) \end{cases} \tag{11}$$

Here, all signals have been notationally simplified (i.e., $v_{\mathrm{CA}}(t)\rightarrow v_{\mathrm{CA}}$) for algebraic clarity. The key modeling challenge lies in the evaluation of cross-terms such as $\langle s_X\cdot i_x\rangle_0$ and $\langle s_X\cdot v_{CX}\rangle_1$, which involve products of non-sinusoidal periodic functions. Based on the harmonic decomposition of both $s_X(t)$ and the dynamic quantities, and in line with [24,25], these products are expanded and defined as follows:

$$\begin{cases} \langle s_X\cdot i_x\rangle_0 = \langle s_X\rangle_0\cdot\langle i_x\rangle_0 + \langle s_X\rangle_{-1}\cdot\langle i_x\rangle_1 + \langle s_X\rangle_1\cdot\langle i_x\rangle_{-1} \\ \langle s_X\cdot v_{CX}\rangle_1 = \langle s_X\rangle_0\cdot\langle v_{CX}\rangle_1 + \langle s_X\rangle_1\cdot\langle v_{CX}\rangle_0 \end{cases} \tag{12}$$

To simplify the model and eliminate unwanted DC biases in the HFT, it is standard to assume

that $\langle s_X \rangle_0 = 0$ [11]. Furthermore, the switching functions' first harmonic components are defined as $<s_A>_1 = -j \cdot 2/\pi$ and $<s_B>_1 = -j \cdot (2/\pi) \cdot e^{-j \cdot \phi(t)}$. Using the symmetry of Fourier coefficients, the conjugate relation $\langle q \rangle_{-1} = \langle q \rangle_1^*$ is used to write:

$$\begin{cases} \langle s_X \cdot i_x \rangle_0 = \langle s_X \rangle_0 \cdot \langle i_x \rangle_0 + \langle s_X \rangle_1^* \cdot \langle i_x \rangle_1 + \langle s_X \rangle_1 \cdot \langle i_x \rangle_1^* \\ \langle s_X \cdot v_{CX} \rangle_1 = \langle s_X \rangle_0 \cdot \langle v_{CX} \rangle_1 + \langle s_X \rangle_1 \cdot \langle v_{CX} \rangle_0 \end{cases} \tag{13}$$

Next, a decomposition of the complex-valued harmonic current into real and imaginary parts takes place: $\langle i_a \rangle_1 = \langle i_a \rangle_1^R + j \cdot \langle i_a \rangle_1^I$, where $R = \Re\{\langle i_a \rangle_1\}$ and $I = \Im\{\langle i_a \rangle_1\}$. After substituting all Fourier components and separating real-valued dynamics, the final GSSA formulation is expressed as shown as follows:

$$\frac{d}{dt}\begin{bmatrix} \langle v_{CA} \rangle_0 \\ \langle i_a \rangle_1^R \\ \langle i_a \rangle_1^I \\ \langle v_{CB} \rangle_0 \end{bmatrix} = \begin{bmatrix} -\frac{1}{R_i \cdot C_A} & 0 & \frac{4}{\pi \cdot C_A} & 0 \\ 0 & -\frac{r_{Lk}}{L_k} & \omega_s & \frac{2 \cdot n \cdot \sin\phi}{\pi \cdot L_k} \\ -\frac{2}{\pi \cdot L_k} & -\omega_s & -\frac{r_{Lk}}{L_k} & \frac{2 \cdot n \cdot \cos\phi}{\pi \cdot L_k} \\ 0 & \frac{4 \cdot n \cdot \sin\phi}{\pi \cdot C_B} & \frac{4 \cdot n \cdot \cos\phi}{\pi \cdot C_B} & -\frac{1}{R_L \cdot C_B} \end{bmatrix} \cdot \begin{bmatrix} \langle v_{CA} \rangle_0 \\ \langle i_a \rangle_1^R \\ \langle i_a \rangle_1^I \\ \langle v_{CB} \rangle_0 \end{bmatrix} + \begin{bmatrix} \frac{1}{R_i \cdot C_A} \\ 0 \\ 0 \\ 0 \end{bmatrix} \cdot \langle v_1 \rangle_0 \tag{14}$$

This model provides a complete description of the 2L-DAB converter dynamics using real- and imaginary-valued state variables, explicitly incorporating the phase-shift angle ϕ at the model level—a significant distinction from the DQ-averaged model in (10), where ϕ emerges only after interpreting power coupling terms.

Figure 4 depicts the equivalent circuit associated with the GSSA model in (14). Structurally, this representation mirrors that of the DQ-based averaged model (Figure 3), comprising two voltage source subcircuits modeling the HFT and two current source subcircuits representing the dynamic behavior of the DC-link capacitors. However, there are key distinctions:

- Voltage channels: The GSSA formulation introduces two orthogonal HFT channels—real and imaginary—where the phase angle ϕ directly modulates the transfer characteristics. The DQ model achieves similar behavior but requires a transformation step and implicit reconstruction of these dynamics through power balances.
- Current coupling: In the GSSA circuit, the HFT's interaction with the DC links is through power-controlled current sources where the in-phase and in-quadrature components (proportional to $\langle i_a \rangle_1^R$ and $\langle i_a \rangle_1^I$, respectively) are directly represented. This yields a cleaner harmonic interpretation and separates dynamic contributions more transparently.
- Emergence of ϕ: A striking feature is the natural appearance of ϕ in the state matrix. In contrast, the DQ model requires an additional derivation step and is less explicit in relating harmonic phase-shifted interactions to physical variables.
- Computational perspective: Though both models are of fourth order, the GSSA approach maintains a strong link to the harmonic structure of switching converters and is particularly beneficial in time-domain simulations where harmonic tracking and waveform reconstruction are critical.

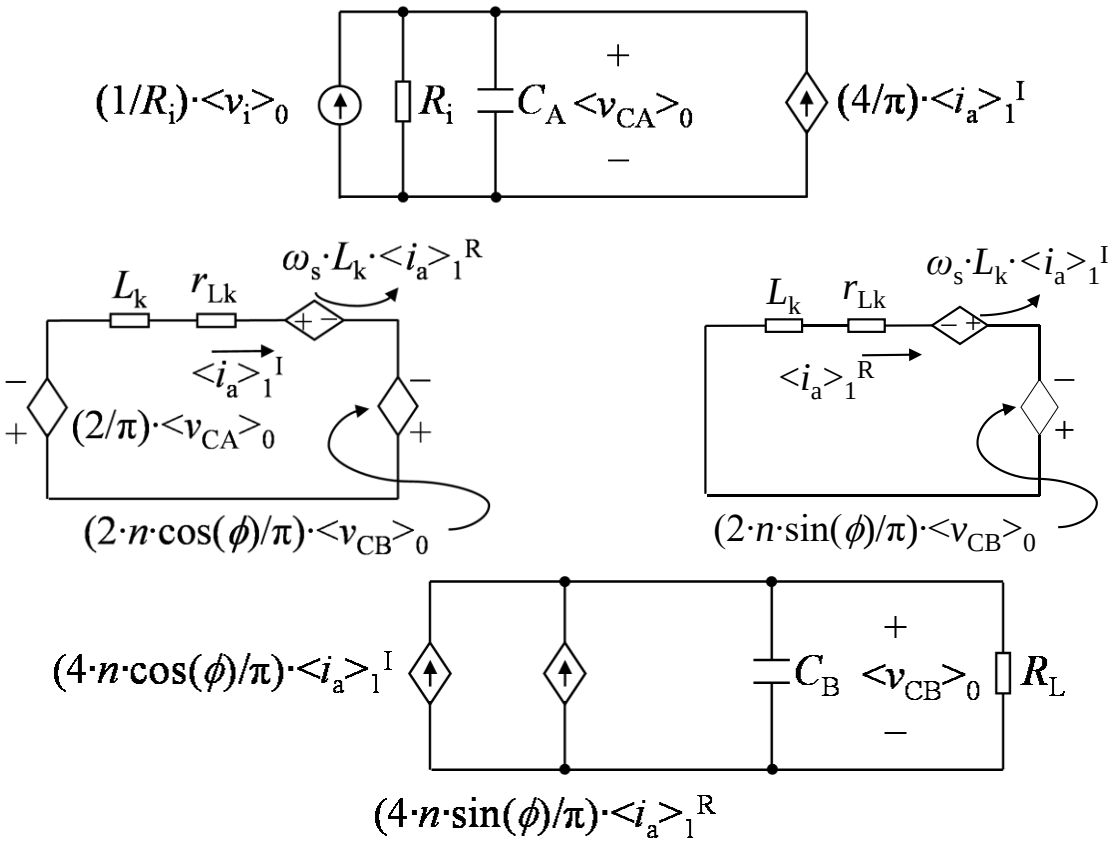

Figure 4. 2L-DAB GSSA model. Model built with two voltage source circuits (that model the transformer) and two current source circuits (that generate the interaction between the system power supply and its output).

In conclusion, the GSSA-based model not only aligns with the DQ-averaged dynamics under steady-state assumptions but also provides a more transparent and harmonically rich representation of the 2L-DAB converter. This makes it a robust alternative for control-oriented analysis and modulation design. Both the DQ-based and GSSA-based models are well-suited for the analysis of this converter, each offering distinct advantages: the DQ model is computationally efficient and intuitive for control synthesis under balanced conditions, while the GSSA model excels in capturing multi-frequency interactions and phase-coupled dynamics with greater fidelity. The choice between them ultimately depends on the analytical goals—whether simplicity and control integration or spectral accuracy and harmonic insight are prioritized.

3.3. Comparison between DQ-based and GSSA averaged models

The averaged modeling of the 2L-DAB converter can be approached using either a DQ-coordinate transformation or a GSSA technique. Both strategies enable the derivation of continuous-time models that abstract the converter's behavior over one switching period, providing valuable insights for dynamic analysis and control-oriented design. However, each method offers distinct advantages depending on the system objectives and analytical requirements.

The DQ-based modeling technique, grounded in the Park transformation, projects the high-

frequency waveforms at the HFT terminals into a rotating reference frame, resulting in a linear and decoupled representation of the converter's fundamental dynamics [23,26]. This transformation explicitly separates the direct (active) and quadrature (reactive) components of voltages and currents, facilitating control synthesis, especially under balanced conditions. Moreover, the DQ model's structure is naturally suited for integration with conventional linear control strategies and frequency-domain techniques such as impedance-based stability analysis and decoupling control design [27].

On the other hand, the GSSA model is derived by decomposing the converter's switching behavior into its dominant harmonic components—typically the zeroth (DC) and first-order (AC) terms—using the Fourier basis. This framework offers an analytically rich and physically interpretable structure, maintaining direct access to both real and imaginary components of the dynamic phasors [7,8,11,24,25]. One of its key strengths lies in its explicit inclusion of the phase-shift angle $\phi(t)$ within the state-space matrices, enabling the modeling of frequency-coupled power transfer and harmonic modulation effects without the need for additional reconstruction steps, as required in the DQ method.

Structurally, both models can be represented using equivalent circuit analogs composed of voltage-source subcircuits (modeling the HFT) and current-source subcircuits (representing the DC-link power exchanges). However, the DQ-based approach achieves this through orthogonal transformations, whereas the GSSA model embeds the harmonic coupling explicitly in its formulation. This makes the GSSA particularly useful for applications involving frequency-domain waveform reconstruction, modulation analysis, and time-varying parameter tracking.

Despite their conceptual differences, both the DQ and GSSA models converge to similar dynamic behavior under steady-state and balanced operating conditions. The GSSA method, however, offers superior resolution of phase and harmonic interactions, making it more accurate in scenarios where high frequency switching harmonics and spectral fidelity are critical. Conversely, the DQ model remains computationally lighter and more intuitive for controller design and system integration.

In conclusion, both modeling strategies are well suited for the analysis and control of the 2L-DAB converter. The choice between them should be based on the analytical objectives: for control design and real-time applications, the DQ model is preferable due to its simplicity and ease of implementation; for harmonic-rich and modulation-sensitive analysis, the GSSA model provides a more complete and physically transparent representation.

3.4. Small-signal linear state-space model

The linearization process in this study is founded upon the dynamic averaged model formulated in the DQ rotating reference frame. This modeling framework is particularly advantageous due to its ability to decouple time-varying sinusoidal steady-state behavior into algebraically manageable DC quantities, thereby facilitating control system design and linear stability analysis.

It is analytically demonstrable that the terminal voltages $v_a(t)$ and $v_b(t)$ of the 2L-DAB converter exhibit square-wave characteristics, with a relative phase shift denoted by $\phi(t)$, which dynamically governs the bidirectional power transfer. As previously discussed, $\phi(t)$ quantifies the instantaneous phase difference between the two FBs and is intrinsically linked to the leakage inductance L_k. This parameter critically affects the energy transfer dynamics and magnetic flux evolution within the HFT

stage, exerting a first-order influence on both the transient and steady-state performance of the converter [1].

Furthermore, from a frequency-domain perspective, the HFT can be equivalently referred to the primary side. In this framework, the output power $P_o(t)$ can be expressed as a function of the phase $\phi(t)$ and the reflected impedance through the leakage reactance X_{Lk}. Consequently, the current flowing from terminal "a" to terminal "b", denoted as $\mathbf{I_a}(j\cdot\omega_s)$, where $\omega_s = 2\cdot\pi/T_s$ is the angular-switching frequency, becomes a key descriptor of the system's energy transfer capability and modulation-dependent behavior [28], as follows:

$$\mathbf{I_a}(j\cdot\omega_s)=\left(\frac{r_{Lk}\cdot V_a}{\left|\mathbf{Z_{L_k}}(j\cdot\omega_s)\right|^2}-\frac{n\cdot V_b\cdot\cos(\phi+\alpha)}{\left|\mathbf{Z_{L_k}}(j\cdot\omega_s)\right|}\right)-j\cdot\left(\frac{X_{Lk}\cdot V_a}{\left|\mathbf{Z_{L_k}}(j\cdot\omega_s)\right|^2}-\frac{n\cdot V_b\cdot\cos(\phi-\beta)}{\left|\mathbf{Z_{L_k}}(j\cdot\omega_s)\right|}\right) \quad (15)$$

In this context, $\mathbf{Z_{Lk}}(j\cdot\omega_s) = r_{LK} + j\cdot X_{Lk}$. Similarly, $X_{Lk} = \omega_s\cdot L_k$. It should be noted that V_a and V_b represent the peak-to-peak voltages of the terminal voltages in frequency domain, $v_a(t)$ and $v_b(t)$, respectively. In contrast, the phase shift angles α and β are defined as follows: $\alpha = \tan^{-1}(X_{Lk}/r_{Lk})$ and $\beta = \tan^{-1}(r_{LK}/X_{Lk})$. Consequently, the expression for $P_o(t)$ is given by $P_o(t) = \mathscr{R}_e\{\mathbf{I_a}^*(j\cdot\omega_s)\cdot\mathbf{V_b}(j\cdot\omega_s)\}$, where:

$$P_o = \frac{n\cdot V_a\cdot V_b\cdot\cos(\phi-\alpha)}{\left|\mathbf{Z_{L_k}}(j\cdot\omega_s)\right|}-\frac{(n\cdot V_b)^2\cdot[\cos\phi\cdot\cos(\phi+\alpha)\ +\ \sin\phi\cdot\cos(\phi-\beta)]}{\left|\mathbf{Z_{L_k}}(j\cdot\omega_s)\right|} \quad (16)$$

From [1], it can be corroborated that a typical waveform for $v_a(t)$ and $v_b(t)$ for this type of converter, according to the dynamics expressed in (5), can be depicted in Figure 5. From Figure 5, it is possible to establish that the square waveforms $v_a(t)$ and $v_b(t)$ are phase-shifted by $\phi(t)$. Additionally, V_{CA} and V_{CB} correspond to the magnitudes of the DC-link voltages on the A and B sides, i.e., $v_{CA}(t) \approx V_{CA}$ and $v_{CB}(t) \approx V_{CB}$, respectively. It is also assumed that $d_A(t)$ of the A-side FB is fixed and set to 50%. This assumption is valid as for the desired operation of the converter, only the B-side FB will be regulated through $\phi(t)$. Therefore, according to (15), it is essential to determine the expressions for $v_a(t)$ and $v_b(t)$ as functions of $\phi(t)$ to understand the dynamics of regulating $P_o(t)$ [28].

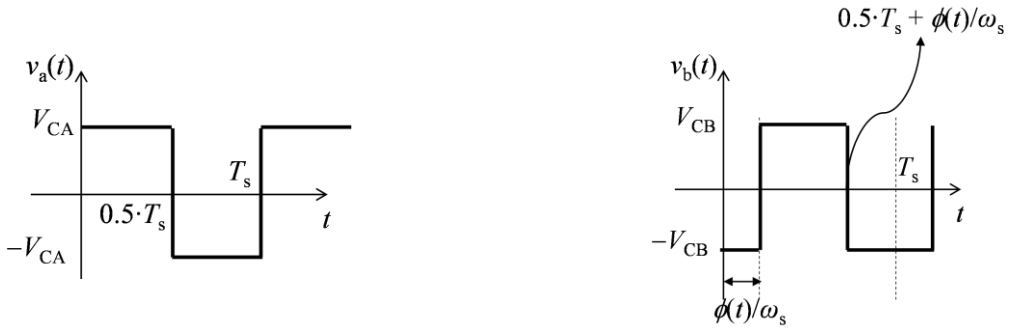

(a) (b)

Figure 5. Square waveforms representing the terminal voltages $v_a(t)$ (a) and $v_b(t)$ (b).

To achieve this, the Fourier series expansion of each of these voltages is generated, yielding the required expressions in terms of the phase shift $\phi(t)$. Thus, it can be verified that this expansion is defined as follows:

$$\begin{cases} v_{a_z}(t) = \dfrac{4}{\pi}\cdot V_{CA}\cdot \sum_{z=1,3,5,\ldots}^{\infty} \dfrac{\sin(z\cdot\omega_s\cdot t)}{z} \\ v_{b_z}(t) = \dfrac{4}{\pi}\cdot V_{CB}\cdot \sum_{z=1,3,5,\ldots}^{\infty} \dfrac{\sin\left(z\cdot\omega_s\cdot t - z\cdot\phi(t)\right)}{z} \end{cases} \tag{17}$$

From here, z is the number of harmonic components of the expansion obtained for $v_a(t)$ and $v_b(t)$. Without loss of generality and to simplify the analysis, it will be assumed that $v_a(t)$ and $v_b(t)$ are defined by their fundamental components, i.e., $v_{a1}(t)$ and $v_{b1}(t)$. According to (10), the expressions for $v_{a1}(t)$ and $v_{b1}(t)$ in D-Q coordinates are required. These conversions are shown as follows [23,29]:

$$\begin{cases} v_{a_1}^{d}(t) = 0 \\ v_{a_1}^{q}(t) = -4/\pi\cdot V_{CA} \\ v_{b_1}^{d}(t) = -4/\pi\cdot V_{CB}\cdot \sin\phi(t) \\ v_{b_1}^{q}(t) = -4/\pi\cdot V_{CB}\cdot \cos\phi(t) \end{cases} \tag{18}$$

Then, by substituting (18) into (10), the large-signal averaged model in D-Q coordinates as a function of $\phi(t)$ is derived and shown as follows:

$$\begin{cases} \dfrac{d\langle v_{CA}(t)\rangle_{T_s}}{dt} = \dfrac{1}{\tau_A}\cdot\left(-\langle v_{CA}(t)\rangle_{T_s} + \langle v_i(t)\rangle_{T_s} - \dfrac{4}{\pi}\cdot V_{CA}\cdot R_i\cdot\dfrac{\langle i_a^q(t)\rangle_{T_s}}{\langle v_{CA}(t)\rangle_{T_s}}\right) \\ \dfrac{d\langle i_a^d(t)\rangle_{T_s}}{dt} = \dfrac{1}{\tau_{HFT}}\cdot\left(-\langle i_a^d(t)\rangle_{T_s} + \omega_s\cdot\tau_{HFT}\cdot\langle i_a^q(t)\rangle_{T_s} + \dfrac{4}{\pi}\cdot n\cdot r_{Lk}\cdot V_{CB}\cdot\sin\langle\phi(t)\rangle_{T_s}\right) \\ \dfrac{d\langle i_a^q(t)\rangle_{T_s}}{dt} = \dfrac{1}{\tau_{HFT}}\cdot\left[-\omega_s\cdot\tau_{HFT}\langle i_a^d(t)\rangle_{T_s} - \langle i_a^q(t)\rangle_{T_s} + \dfrac{4}{\pi}\cdot r_{Lk}\cdot V_{CB}\cdot\cos\langle\phi(t)\rangle_{T_s}\right] \\ \dfrac{d\langle v_{CB}(t)\rangle_{T_s}}{dt} = \dfrac{1}{\tau_B}\cdot\left(-\langle v_{CB}(t)\rangle_{T_s} - \dfrac{4}{\pi}\cdot n\cdot V_{CB}\cdot R_L\cdot\left(\dfrac{\sin\langle\phi(t)\rangle_{T_s}\cdot\langle i_a^d(t)\rangle_{T_s} + \cos\langle\phi(t)\rangle_{T_s}\cdot\langle i_a^q(t)\rangle_{T_s}}{\langle v_{CB}(t)\rangle_{T_s}}\right)\right) \end{cases} \tag{19}$$

Finally, for system linearization, steady-state values are calculated. By setting the derivatives in (19) to zero and treating $I_a^{\,d}$, $I_a^{\,q}$, and φ as unknowns, with the remaining terms considered known, the equilibrium points are obtained by solving the following equation system:

$$\begin{cases} -V_{CA} + V_i - 4/\pi\cdot R_i\cdot I_a^q = 0 \\ -I_a^d + \omega_s\cdot\tau_{HFT}\cdot I_a^q + 4/\pi\cdot n\cdot r_{Lk}\cdot V_{CB}\cdot\sin\varphi = 0 \\ \omega_s\cdot\tau_{HFT}\cdot I_a^d - I_a^q - 4/\pi\cdot r_{Lk}\cdot V_{CA} + 4/\pi\cdot n\cdot r_{Lk}\cdot V_{CB}\cdot\cos\varphi = 0 \\ -V_{CB} - 4/\pi\cdot n\cdot R_L\cdot\left(I_a^d\cdot\sin\varphi + I_a^q\cdot\cos\varphi\right) = 0 \end{cases} \tag{20}$$

Considering the equilibrium points calculated in (20) (capital letters), applying a Taylor series expansion, and perturbing the variables, the small-signal linear state-space model is derived as follows [25]:

$$\begin{cases} \dfrac{d\mathbf{x}(t)}{dt} = \mathbf{A}\cdot\mathbf{x}(t) + \mathbf{B}\cdot\mathbf{u}(t) \\ y(t) = \mathbf{C}\cdot\mathbf{x}(t) + \mathbf{D}\cdot\mathbf{u}(t) \end{cases} \tag{21}$$

From here, $\mathbf{x}(t) = [\hat{v}_{CA}(t),\ \hat{i}_a^d(t),\ \hat{i}_a^q(t),\ \hat{v}_{CB}(t)]^T$, $\mathbf{u}(t) = [\hat{v}_i(t),\ \hat{\phi}_i(t)]^T$, and $y(t) = \hat{v}_{CB}(t)$

represent the state vector, the input vector, and the scalar output, respectively. Symbolically, $\mathbf{x}(t) \in \{\mathbb{R}^4\}$, $\mathbf{u}(t) \in \{\mathbb{R}^2\}$, and $y(t) \in \{\mathbb{R}\}$. Additionally, **A**, **B**, **C**, and **D** are the state, input, output, and direct transmission matrices, respectively, defined as follows:

$$\mathbf{A} = \begin{bmatrix} k_{11} & 0 & k_{31} & 0 \\ 0 & k_{12} & k_{22} & 0 \\ 0 & k_{13} & k_{23} & 0 \\ 0 & k_{24} & k_{34} & k_{14} \end{bmatrix}, \ \mathbf{B} = \begin{bmatrix} k_{21} & 0 \\ 0 & k_{32} \\ 0 & k_{33} \\ 0 & k_{44} \end{bmatrix}, \tag{22}$$

$$\mathbf{C} = [0 \quad 0 \quad 0 \quad 1], \mathbf{D} = \mathbf{0}_{1x2}$$

Symbolically, $\mathbf{A} \in \mathscr{M}_{4x4}\{\mathrm{K}\}$, $\mathbf{B} \in \mathscr{M}_{4x2}\{\mathrm{K}\}$, $\mathbf{C} \in \mathscr{M}_{1x4}\{\mathrm{K}\}$, and $\mathbf{D} \in \mathscr{M}_{1x2}\{\mathrm{K}\}$. All constants *k*s are defined as follows:

$$\begin{cases} k_{11} = 1/\tau_{\mathrm{A}} \cdot (-1 + 4/\pi \cdot R_{\mathrm{i}} \cdot I_{\mathrm{a}}^{\mathrm{q}}/V_{\mathrm{CA}}) \\ k_{21} = 1/\tau_{\mathrm{A}} \\ k_{31} = -4/\pi \cdot R_{\mathrm{i}}/\tau_{\mathrm{A}} \\ k_{12} = -1/\tau_{\mathrm{HFT}} \\ k_{22} = -\omega_{\mathrm{s}} \\ k_{32} = 4/\pi \cdot n \cdot r_{\mathrm{Lk}} \cdot V_{\mathrm{CB}} \cdot \cos\varphi/\tau_{\mathrm{HFT}} \\ k_{13} = -\omega_{\mathrm{s}} \\ k_{23} = k_{12} \\ k_{33} = 4/\pi \cdot n \cdot r_{\mathrm{Lk}} \cdot V_{\mathrm{CB}} \cdot \sin\varphi/\tau_{\mathrm{HFT}} \\ k_{14} = -1/\tau_{\mathrm{A}} \cdot \left(-1 + 4/\pi \cdot n \cdot R_{\mathrm{L}} \cdot \left(I_{\mathrm{a}}^{\mathrm{d}} \cdot \sin\varphi/V_{\mathrm{CB}} + I_{\mathrm{a}}^{\mathrm{q}} \cdot \cos\varphi/V_{\mathrm{CB}}\right)\right) \\ k_{24} = -4/\pi \cdot n \cdot R_{\mathrm{L}} \cdot \sin\varphi/\tau_{\mathrm{B}} \\ k_{24} = -4/\pi \cdot n \cdot R_{\mathrm{L}} \cdot \cos\varphi/\tau_{\mathrm{B}} \\ k_{44} = -4/\pi \cdot n \cdot R_{\mathrm{L}} \cdot \left(I_{\mathrm{a}}^{\mathrm{d}} \cdot \cos\varphi - I_{\mathrm{a}}^{\mathrm{q}} \cdot \sin\varphi\right)/\tau_{\mathrm{B}} \end{cases} \tag{23}$$

4. Control system description

This section analyzes the control strategy for the 2L-DAB converter in the D-Q rotating reference frame. The main goal is to regulate the output voltage $v_{\mathrm{CB}}(t)$, which affects power transfer between the A and B sides. Using the derived small-signal linear model, a controller will be designed to manage the phase shift $\phi(t)$ at the B-side FB. The analysis will include considerations of stability, transient response, and robustness under varying conditions, ensuring effective control in both steady-state and dynamic scenarios.

Next, based on (21), the model of the converter in the complex variable domain (s) is obtained from:

$$Y(\mathrm{s})/\mathbf{U}(\mathrm{s}) = [\mathbf{C} \cdot (s \cdot \mathbf{I}_4 - \mathbf{A})^{-1} \cdot \mathbf{B} + \mathbf{D}] \tag{24}$$

where $Y(s) = V_{\mathrm{CB}}(s)$ is the complex scalar output variable and $\mathbf{U}(s) = [V_{\mathrm{i}}(s), \varphi(s)]^{\mathrm{T}}$ is the complex input vector. Symbolically, $\mathbf{U}(s) \in \{\mathbb{C}^2\}$ and $Y(s) \in \{\mathbb{C}\}$.

Figure 6 presents the proposed control diagram for this converter, which is based on the linear model in D-Q coordinates. Thus, by designing the compensator within this model, an appropriate regulator design is achieved for implementation in the switched model of the converter as defined in (6).

The control loop is primarily structured around a PI compensator. This compensator operates by processing the error signal, obtained from the deviation between the reference output voltage $\hat{v}_{\mathrm{CB}}^{*}(t)$ and the actual measured output voltage $\hat{v}_{\mathrm{CB}}(t)$. Through its proportional and integral actions, the PI compensator generates the control effort in the form of a phase-shift signal, $\hat{\phi}(t)$. This phase-shift waveform directly interfaces with the linearized plant model defined in the D-Q reference frame, ensuring precise modulation of the converter dynamics to achieve the desired steady-state and transient performance objectives.

The compensator design procedure is based on analyzing the open-loop gain $T(s)$ through the Bode plot of the open-loop transfer function (TF) $T_{\mathrm{u}}(s)$, which characterizes the plant dynamics to be controlled [25]. The objective is to tune the PI compensator such that the crossover frequency of $T_{\mathrm{u}}(s)$, denoted as f_{c}, is aligned with the converter's switching frequency f_{s} [25].

Given that f_{s} is typically high in most practical applications, designing the compensator around this frequency effectively enhances disturbance rejection in the control loop, ensuring a minimal relative steady-state error [26]. The system's open-loop TF is parameterized by the open-loop gain k_{u}, along with the system's zeros z_x and poles p_y, where $x \in \{1, 2\}$ and $y \in \{1, 2, 3\}$.

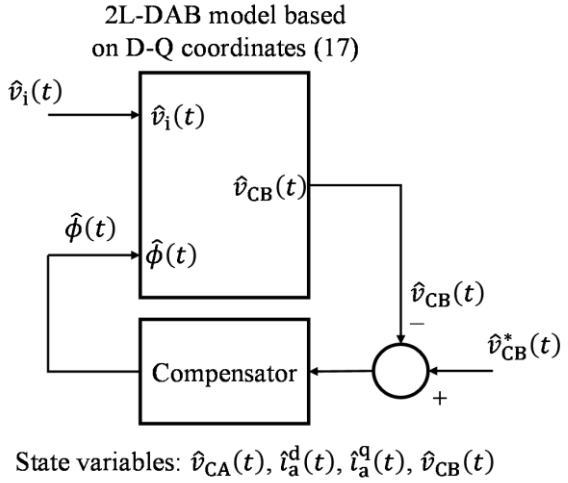

Figure 6. Proposed control diagram based on the linear model in D-Q coordinates (17).

To verify the stability of the compensator, the phase-margin test (PMT) theorem is employed, providing a rapid assessment of whether all system poles remain in the left half of the s-plane, ensuring a stable response [26]. The $T_{\mathrm{u}}(s)$, derived from (24), represents the system's output control transfer function and is expressed as follows:

$$T_{\mathrm{u}}(s) = -k_{\mathrm{u}} \cdot \frac{(s+z_1)\cdot(s+z_2)}{(s+p_{11})\cdot(s+p_{21}+\mathrm{j}\cdot p_{31})\cdot(s+p_{21}-\mathrm{j}\cdot p_{31})} \tag{25}$$

The simulated system parameters are detailed in Table 1, which includes values for key components such as the DC-link capacitors, load resistance, leakage inductance, and their associated parasitic. The A-side DC-link voltage source $v_{\mathrm{i}}(t)$ is set to 800 V, with a switching frequency of 100 kHz. The converter is initialized in a de-energized state, with all variables set to zero. By utilizing these parameters and computing (24), the evaluated form of (25) is obtained. Subsequently, the Bode diagram of (25) is computed and presented in Figure 7 (blue curve).

Table 1. Model parameters.

Parameter	Values
R_i	10 [mΩ]
$C_a = C_b$	200 [μF]
R_L	50 [Ω]
L_k	16 [μH]
r_{Lk}	1 [mΩ]
n	1

From Figure 7, it is evident that $T_u(s)$ does not exhibit a crossover frequency f_c near the switching frequency f_s (yellow line). This confirms the necessity of a compensator to modify the system's frequency response, effectively shifting the curve to align f_c with f_s, thereby enhancing system performance and stability. The TF of the PI-type compensator can be described as:

$$C(s) = k_p \cdot (1 + \omega_L / s) \tag{26}$$

where k_p and ω_L are the proportional gain and the integral crossover frequency, respectively. It should be noted that since f_L is significantly lower than f_c, the phase margin remains unaffected. Consequently, at low frequencies, the inverse term $1/s$ in the compensator enforces an integral action, ensuring the elimination of steady-state error by continuously integrating the error signal. This characteristic allows the system to maintain zero steady-state error while preserving the desired dynamic response.

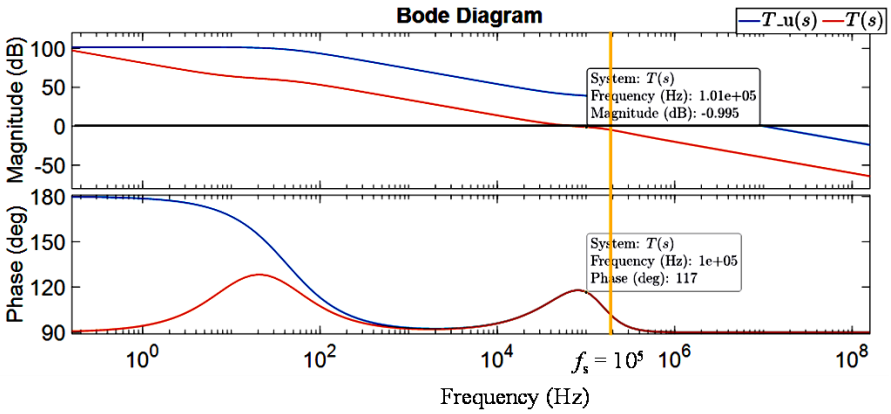

Figure 7. Bode diagram of $T(s)$ (blue) and $Tu(s)$ (red). Switching frequency in yellow line.

Considering (25) and (26), the closed-loop transfer function $T(s)$ can be derived and expressed as:

$$\mathrm{T}(s) = -k_u \cdot \frac{(s + z_1)\cdot(s + z_2)\cdot\left(1 + \frac{\omega_L}{s}\right)}{(s + p_{11})\cdot(s + p_{21} - \mathrm{j}\cdot p_{31})\cdot(s + p_{21} + \mathrm{j}\cdot p_{31})} \tag{27}$$

where k_u is the converter gain, the z_1 and z_2 are the converter zeros, p_{11} is the real pole, and $p_{21} \pm \mathrm{j}\cdot p_{31}$ represent a pair of complex conjugate poles.

This expression describes the system's closed-loop behavior, incorporating both real and complex-conjugate poles that define the system's stability and transient response. The placement of

these poles and zeros significantly impacts performance metrics such as overshoot, settling time, and damping ratio [27].

According to the values in Table 1, the computed values of the system gains, zeros, and poles are summarized in Table 2.

Table 2. Values of the system gains, zeros, and poles.

Parameter	Values
k_u	$6.4299 \cdot 10^7$
z_1	$6.604 \cdot 10^5$
z_2	$5.896 \cdot 10^5$
p_{11}	267.5
p_{21}	$625 \cdot 10^3$
p_{31}	$628.311 \cdot 10^3$

These values characterize the system's frequency response and stability properties. The placement of the poles and zeros in the *s*-plane determines key dynamic attributes, such as bandwidth, phase margin, and transient response performance [27].

For the purpose of calculating k_p, it can be selected to achieve the desired crossover frequency f_c. If k_u is approximated to its asymptotic behavior at high frequencies, then at high frequencies, the closed-loop transfer function $T(s)$ can be expressed as [25]:

$$\|\mathbf{T}(j\cdot\omega)\|_{\omega\to\infty} \approx \frac{\omega\cdot k_p}{k_u} \Rightarrow \|\mathbf{T}(j\cdot\omega)\|_{\omega=\omega_s} = 1 \Rightarrow k_p \approx \frac{k_u}{\omega_s} \tag{28}$$

On the other hand, the low-frequency corner f_L is chosen to be sufficiently lower than f_c to maintain an adequate phase margin [26]. Specifically, it is set as:

$$f_L = (1/1{,}000)\cdot f_c \tag{29}$$

which ensures that the compensator introduces minimal phase shift at the gain crossover frequency, preserving stability [26]. In terms of angular frequency:

$$\omega_L = 2\cdot\pi\cdot f_L \tag{30}$$

This selection guarantees that the integral action of the PI compensator effectively mitigates steady-state error while avoiding excessive phase lag at higher frequencies.

The stability of the compensated system is determined by the location of the poles in the *s*-plane [27,28]. A stable system requires all poles to be in the left half-plane (i.e., they must have negative real parts). The root locus plot regarding $T(s)$ is showing in Figure 8. From Figure 8, the dominant poles of the system are the complex conjugate pair. These poles have a high damping factor, indicating an adequately damped response with minimal oscillatory behavior. Additionally, all other poles are located in the left half-plane, except for a single pole at the origin.

The presence of a pole suggests that the system exhibits a marginally stable behavior due to the integral action of the PI compensator. This is expected, as the integral term ensures zero steady-state error but does not contribute additional damping. The compensator design ensures that all dominant poles remain in the left half-plane, maintaining system stability while achieving precise output regulation [27,28].

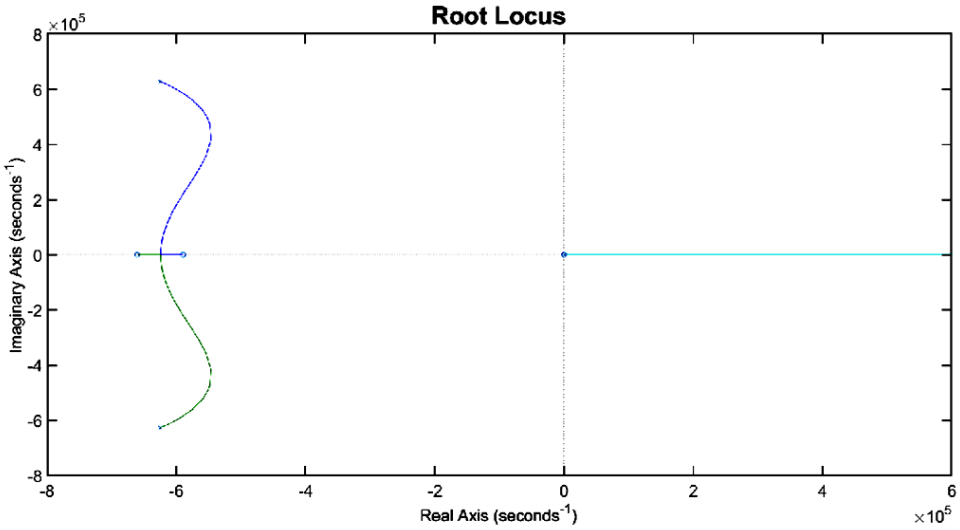

Figure 8. Root locus plot of the compensated transfer function $T(s)$. The plot clearly demonstrates that all poles and zeros are positioned in the left half of the s-plane, verifying the system's stability and ensuring a well-damped response.

To further validate the stability of the system, the phase margin and gain margin are analyzed from the Bode plot of the closed-loop TF in (27). The phase margin (ϕ_m) is a key indicator of system robustness, representing the additional phase lag required to bring the system to the verge of instability. From the frequency domain analysis [25,27]:

- Phase margin: $\phi_m = 297$ °.
- Gain margin: Sufficiently high (indicating strong stability).

A significantly high phase margin ensures that the system can tolerate parameter variations and external disturbances without compromising stability. This elevated phase margin validates that the compensator design effectively enhances both damping and transient performance, as supported in [25,27].

5. Sensitivity of poles to parameter variations

To perform the sensitivity analysis of the controller and analyze the impact of system parameter variations on the performance of the closed-loop system, the focus should be on the closed-loop TF in (27). This equation defines the closed-loop dynamics, and its sensitivity to parameter variations can be analyzed by considering the key system parameters that affect the poles and zeros.

5.1. Small-signal linear state-space model

The system's stability and transient response are primarily influenced by the location of its poles. Since these poles depend on system parameters, their sensitivity can be examined by differentiating the characteristic equation of $T(s)$ with respect to each parameter [29].

The characteristic equation of $T(s)$ is:

$$D(s) = (s + p_{11})\cdot(s + p_{21} - j\cdot p_{31})\cdot(s + p_{21} + j\cdot p_{31}) \tag{31}$$

To quantify the influence of a system parameter (parameter vector) $\mathbf{g} = [L_k, C_A, C_B, R_L]^T$, where $\mathbf{g} \in \{\mathbb{R}^4\}$ on pole locations, the sensitivity function is defined as follows [29]:

$$S_{p_{y1}}^{\mathbf{g}} = \frac{\partial p_{y1}}{\partial \mathbf{g}}, \forall\, y \in \{1,2,3\} \tag{32}$$

After computing (32), a ±10% variation is applied to each parameter in **g**, and the corresponding root locus diagrams of $T(s)$ are generated, as shown in Figure 9. Figures 9(a) and 9(b) illustrate the root locus variations for L_k, Figures 9(c) and (d) correspond to C_A, Figures 9(e) and (f) correspond to C_B, and Figures 9(g) and (h) correspond to R_L.

A visual inspection of Figure 9 confirms that the compensator maintains proper regulation across all cases, ensuring stable converter operation. The poles and zeros remain largely unchanged for variations in C_A, C_B, and R_L, indicating robustness to these parameters. In contrast, variations in L_k slightly shift the pole-zero locations, but all poles remain in the left half-plane, preserving system stability.

6. Simulation results

This section presents a detailed assessment of the simulation results obtained for the 2L-DAB converter configuration shown in Figure 1. The simulations were carried out using MATLAB-Simulink. Also, three complementary models were used to evaluate the dynamic behavior of the system:

- The switching model, defined by the set of differential equations in (6).
- The large-signal averaged model in D-Q coordinates, as presented in (10).
- The large-signal averaged model based on GSSA, formulated in (14).

To ensure a consistent and fair comparative analysis across all modeling strategies, the variables derived from the D-Q domain are transformed back into their original electrical coordinate system before simulation.

6.1. Dynamic simulation scenarios

The converter is initialized with an output voltage reference $v_L(t) = 800$ V, and all internal state variables (capacitor voltages, inductor currents, and phase angle) are set to zero to reflect a cold-start operating condition. Two primary disturbances are introduced sequentially to evaluate system performance under dynamic transitions:

1. At $t = 0.3$ s, a step-down perturbation is applied to the output voltage reference, decreasing it from $v_L^*(t) = 800$ V to $v_L^*(t) = 400$ V.
2. Subsequently, at $t = 0.5$ s, a load disturbance is imposed by reducing the load resistance R_L by 60%, effectively changing its value from $R_L = 75\ \Omega$ to $R_L = 30\ \Omega$.

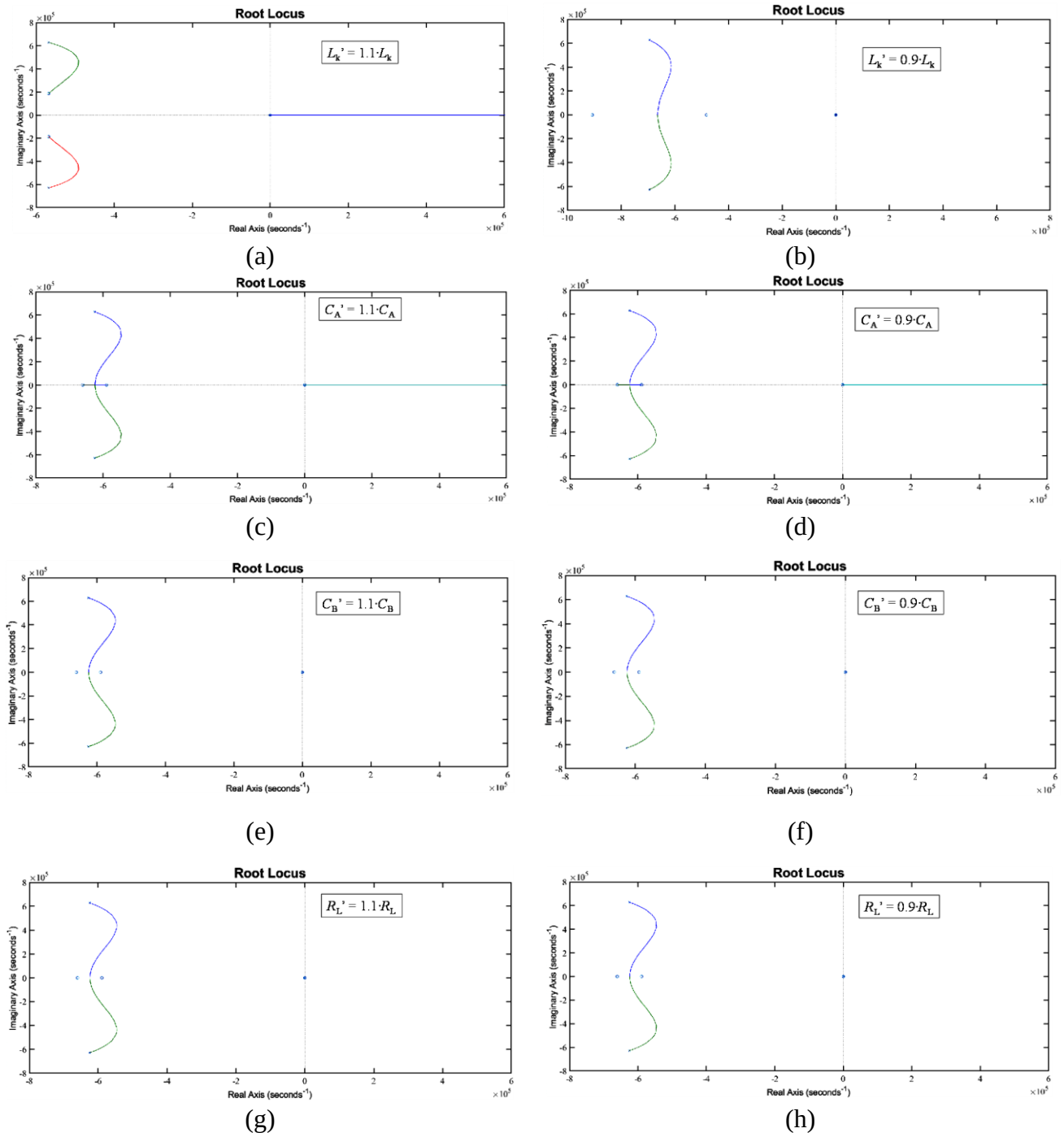

Figure 9. Root locus plots of $T(s)$ for sensitivity analysis under ±10% variations in system parameters: (a)–(b) L_k; (c)–(d) C_A; (e)–(f) C_B; and (g)–(h) R_L.

6.2. Simulation outcomes

Figure 10 presents the time-domain trajectories of key system variables as observed through three distinct modeling frameworks:

- The switching model, annotated with the subscript "sw",
- The large-signal averaged model in D-Q coordinates, denoted by "av", and

• The averaged model based on GSSA, indicated by "GSSA".

The variables analyzed include the output load voltage $v_L(t)$, the A-side DC-link capacitor voltage $v_{CA}(t)$, the leakage inductance current $i_a(t)$, the phase shift angle $\phi(t)$ across the HFT, and the primary-side and secondary-side transformer voltages $v_a(t)$ and $v_b(t)$, respectively. These variables are systematically displayed in Figures 10(a)–(f).

To facilitate detailed analysis, zoomed-in segments are incorporated within Figures 10(a), (b), and (d), focusing on the system's response during critical transitions—specifically the voltage reference step at t = 0.3 s and the load disturbance at t = 0.6 s. These magnified views provide high-resolution insights into the closed-loop control dynamics, allowing for precise evaluation of regulation performance and disturbance rejection capability.

In addition, Figure 11 expands the scope of the analysis by presenting the HFT dynamics in the D-Q reference frame. The depicted variables include the D- and Q-axis components of the A-side transformer voltage $v_a^d(t)$, $v_a^q(t)$, the B-side transformer voltage $v_b^d(t)$, $v_b^q(t)$, and the transformer current $i_a^d(t)$, $i_a^q(t)$, as shown in Figures 11(a)–(c), respectively.

Two distinct perturbations are introduced to the D-Q domain signals: the first at t = 0.3 s and the second at t = 0.6 s, targeting specific voltage and current components. As in Figure 10, zoomed-in segments are included to enhance the visibility of transient phenomena. These detailed views expose the system's immediate response and convergence characteristics under D-Q transformation, emphasizing the fidelity and robustness of the D-Q modeling framework in capturing and predicting converter dynamics under realistic operating conditions.

6.3. Performance metrics and observations

Table 3 quantifies three essential figures of merit (FoMs) for both the switching and averaged models: the overshoot magnitude M_p (%), the settling time t_s (s), and the steady-state error e_{ss} (%).

The results clearly validate the control system's robustness, as all FoMs remain within acceptable thresholds across the switching and averaged models. The high fidelity of the D-Q and GSSA models in replicating the switching behavior confirms their utility for control-oriented analysis and offline design validation.

6.4. Model validation

The simulation results in Figures 10–11 and Table 3 establish a strong correlation between the switching model and its two averaged counterparts—DQ and GSSA. Both averaged models succeed in eliminating high-frequency ripple components while preserving the fundamental dynamic characteristics of the system. The observed discrepancies between DQ and GSSA results are minimal, with a maximum deviation below 1%, thus confirming their near equivalence in both transient and steady-state conditions.

Additionally, the D-Q model for the HFT variables (Figure 11) demonstrates remarkable consistency in both accuracy and response speed. The D-Q framework captures the transient phase trajectories and steady-state convergence with high fidelity, particularly in the presence of step disturbances in control and load parameters. Its ability to preserve dynamic alignment with the switching model while significantly reducing simulation complexity and computation time makes it a powerful tool for model-based design.

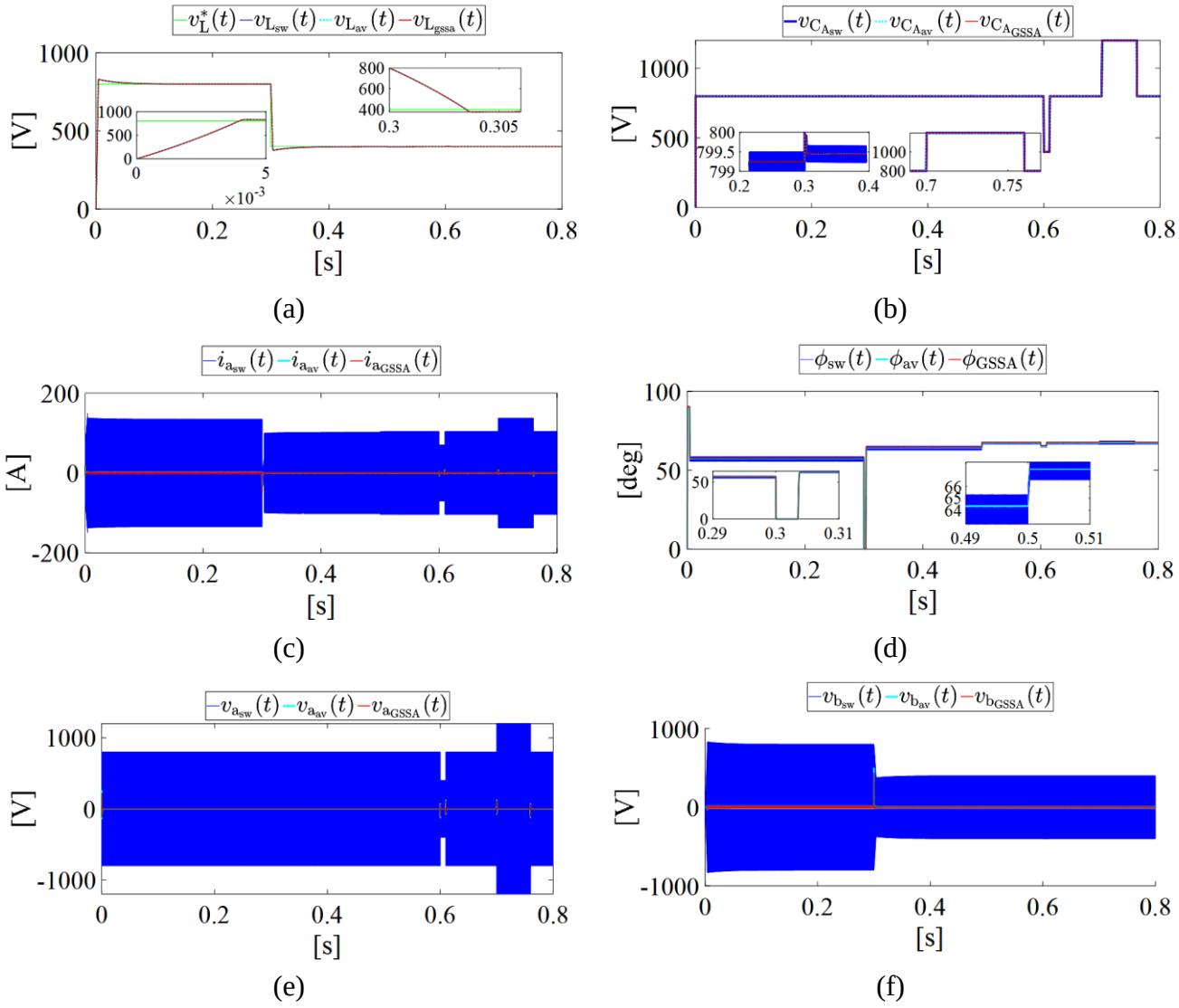

Figure 10. Simulation results under transients of the dynamic variables of interest of the converter. Zero initial conditions. Step change in $v_L(t)$ at 0.3 s. The variables belonging to the switching model are those with the subscript "sw". Those belonging to the D-Q coordinate averaged model have the subscript "av". Those belonging to the averaged model based on GSSA have the subscript "GSSA". (a) $v_L(t)$. (b) $v_{CA}(t)$. (c) $i_a(t)$. (d) $\phi(t)$. (e) $v_a(t)$. (f) $v_b(t)$.

Finally, the successful validation of the large-signal averaged models underscores their practical applicability in advanced control system development, real-time implementation strategies, and embedded system simulation environments. These models offer a trade-off between accuracy and computational efficiency, making them ideal candidates for predictive control synthesis, hardware-in-the-loop testing, and converter optimization workflows.

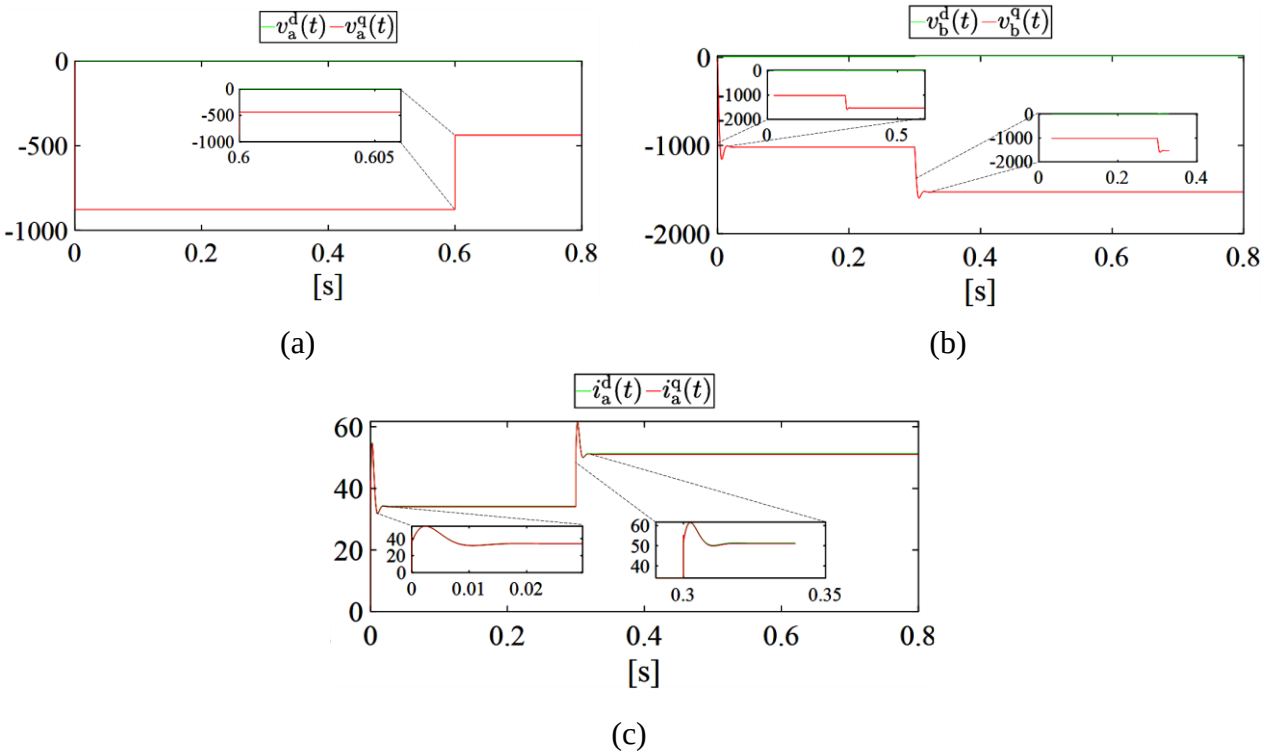

Figure 11. Simulation results under transient of the HFT variables in D-Q coordinates. Disturbances in $v_{ad}(t)$ at 0.6 s and in $v_{bq}(t)$, $i_{ad}(t)$, and $i_{aq}(t)$ at 0.3 s. (a) $v_{ad}(t)$ and $v_{aq}(t)$. (b) $v_{bd}(t)$ and $v_{bq}(t)$. (c) $i_{ad}(t)$ and $i_{aq}(t)$.

Table 3. Figure of merit results for switching and averaged models (DQ/GSSA).

Model	FoM	$v_L(t)$
Switching	M_p (%)	4 at start up; 6.2 at 0.3 s
	t_s (s)	0.1; 0.08
	e_{ss} (%)	~ 0
Average (DQ/GSSA)	M_p (%)	4 at start up; 6.1 at 0.3 s
	t_s (s)	0.1; 0.08
	e_{ss} (%)	~ 0

7. Conclusions

This research presented a multifaceted study on the modeling, analysis, and control of a two-level dual active bridge (2L-DAB) DC–DC converter. The converter was described through three distinct modeling approaches: the switching model, a large-signal DQ-averaged model, and a generalized state-space averaging (GSSA) model. Each formulation offered unique insights and computational tools tailored to specific aspects of the converter's dynamic behavior, performance evaluation, and control system design.

The switching model established the fundamental nonlinear time-domain dynamics of the 2L-DAB system, preserving the full detail of instantaneous switching events, duty-cycle modulation, and phase-shift interactions. This model served as a baseline for validating the accuracy of the reduced-order averaged models and allowed for high-fidelity simulations under transient

disturbances.

The DQ-domain large-signal model was derived by applying the Park transformation to the converter equations, resulting in a coordinate-decoupled formulation suitable for real-time control and system analysis. This model enabled the derivation of a linearized small-signal state-space representation around an operating point. The linearized model was then used to design proportional-integral controllers using loop gain analysis and the phase margin test, which ensured the required phase margin and gain crossover frequency for dynamic stability. The resulting closed-loop system was tested against reference and load perturbations, demonstrating its ability to regulate the output voltage while maintaining desirable transient behavior in terms of overshoot, settling time, and steady-state error.

In parallel, a GSSA model was formulated to capture the converter's frequency-domain structure through harmonic decomposition. Unlike traditional averaged models, the GSSA technique revealed the spectral content of the internal states and the impact of the phase-shift angle $\phi(t)$ directly in the system dynamics. This formulation provided access to harmonic-domain ripple information and allowed for evaluating spectral components that are completely averaged out in the DQ-domain representation. The GSSA model offered a complementary view that is particularly valuable for understanding power coupling, interharmonic interactions, and high-frequency ripple propagation in the converter's operation.

The comparative analysis between the DQ and GSSA models was conducted by subjecting both to identical simulation scenarios involving dynamic disturbances. Results confirmed that the DQ-domain model is efficient for control-oriented tasks and compact implementation, providing fast simulation times and reduced computational complexity. In contrast, the GSSA model demonstrated superior capability in capturing steady-state harmonic distortion, frequency-selective behavior, and waveform reconstruction.

Overall, this study establishes a complete and consistent framework for the modeling and control of 2L-DAB converters. It highlights the importance of choosing the appropriate modeling technique depending on the application context—control design, stability analysis, or harmonic assessment—and sets a solid foundation for future investigations into advanced modulation and control strategies, such as model predictive control or adaptive nonlinear control.

Author contributions

Conceptualization, J.M.C.-S.; methodology, J.M.C.-S., R.R., F.S., J.L.A.-L, and N.K.; validation, J.M.C.-S., R.R., F.S., J.L.A.-L, and N.K.; formal analysis, J.M.C.-S., R.R., F.S., J.L.A.-L, and N.K.; investigation, J.M.C.-S., R.R., F.S., J.L.A.-L, and N.K.; writing—original draft preparation, J.M.C.-S.; writing—review and editing, J.M.C.-S., R.R., F.S., J.L.A.-L, and N.K.; supervision, J.M.C.-S.

Use of Generative-AI tools declaration

The authors declare they have not used Artificial Intelligence (AI) tools in the creation of this article.

Conflict of interest

The authors declare there is no conflict of interest in this paper.

References

1. De Doncker, RWAA, Divan DM, Kheraluwala MH (1991) A Three-Phase Soft-Switched High-Power-Density DC/DC Converter for High-Power Applications. *IEEE T Ind Appl* 27: 63–73. https://doi.org/10.1109/28.67533
2. Demetriades GD (2005) On Small-Signal Analysis and Control of the Single- and the Dual-Active Bridge Topologies.
3. Kheraluwala MN, Gascoigne RW, Divan DM, Baumann ED (1992) Performance Characterization of a High-Power Dual Active Bridge DC-to-DC Converter. *IEEE T Ind Appl* 28: 1294–1301. https://doi.org/10.1109/28.175280
4. Rodríguez Alonso AR, Sebastian J, Lamar DG, Hernando MM, Vazquez A (2010) An Overall Study of a Dual Active Bridge for Bidirectional DC/DC Conversion. In *Proceedings of the 2010 IEEE Energy Conversion Congress and Exposition*, 1129–1135. https://doi.org/10.1109/ECCE.2010.5617847
5. Krismer F, Kolar JW (2010) Accurate Power Loss Model Derivation of a High-Current Dual Active Bridge Converter for an Automotive Application. *IEEE T Ind Electron* 57: 881–891. https://doi.org/10.1109/TIE.2009.2025284
6. Rodríguez A, Vázquez A, Lamar DG, Hernando MM, Sebastián J (2015) Different Purpose Design Strategies and Techniques to Improve the Performance of a Dual Active Bridge with Phase-Shift Control. *IEEE T Power Electr* 30: 790–804. https://doi.org/10.1109/TPEL.2014.2309853
7. Rolak M, Twardy M, Soból C (2022) Generalized Average Modeling of a Dual Active Bridge DC-DC Converter with Triple-Phase-Shift Modulation. *Energies* 15: 6092. https://doi.org/10.3390/en15166092
8. Qin H, Kimball JW (2012) Generalized Average Modeling of Dual Active Bridge DC–DC Converter. *IEEE T Power Electr* 27: 2078–2084. https://doi.org/10.1109/TPEL.2011.2165734
9. George K (2015) Design and Control of a Bidirectional Dual Active Bridge DC-DC Converter to Interface Solar, Battery Storage, and Grid-Tied Inverters. *Electrical Engineering Undergraduate Honors Theses*.
10. Rodriguez-Rodriguez JR, Salgado-Herrera NM, Torres-Jimenez J, Gonzalez-Cabrera N, Granados-Lieberman D, Valtierra-Rodriguez M (2021) Small-Signal Model for Dual-Active-Bridge Converter Considering Total Elimination of Reactive Current. *J Mod Power Syst Clean Energy* 9: 450–458. https://doi.org/10.35833/MPCE.2018.000911
11. Liu B, Davari P, Blaabjerg F (2020) An Enhanced Generalized Average Modeling of Dual Active Bridge Converters. In *Proceedings of the 2020 IEEE Applied Power Electronics Conference and Exposition (APEC)*, 85–90. https://doi.org/10.1109/APEC39645.2020.9124001
12. He J, Chen Y, Lin J, Chen J, Cheng L, Wang Y (2023) Review of Modeling, Modulation, and Control Strategies for the Dual-Active-Bridge DC/DC Converter. *Energies* 16: 6646. https://doi.org/10.3390/en16186646
13. Shao S, Chen L, Shan Z, Gao F, Chen H, Sha D, Dragičević T (2022) Modeling and Advanced Control of Dual-Active-Bridge DC–DC Converters: A Review. *IEEE T Power Electr* 37: 1524–1547. https://doi.org/10.1109/TPEL.2021.3108157
14. Shah SS, Bhattacharya S (2017) Large & Small Signal Modeling of Dual Active Bridge Converter Using Improved First Harmonic Approximation. In *Proceedings of the 2017 IEEE*

Applied Power Electronics Conference and Exposition (APEC), 1175–1182. https://doi.org/10.1109/APEC.2017.7930844
15. Ghazal OM, Marei MI, Mohamad AMI (2024) Small-Signal Modeling Comparison of Dual Active Bridge Converter. *e-Prime - Advances in Electrical Engineering, Electronics and Energy* 8: 100570. https://doi.org/10.1016/j.prime.2024.100570
16. Shao S, Chen H, Wu X, Zhang J, Sheng K (2019) Circulating Current and ZVS-on of a Dual Active Bridge DC-DC Converter: A Review. *IEEE Access* 7: 50561–50572. https://doi.org/10.1109/ACCESS.2019.2911009
17. Wang P, Chen X, Tong C, Jia P, Wen C (2021) Large- and Small-Signal Average-Value Modeling of Dual-Active-Bridge DC–DC Converter with Triple-Phase-Shift Control. *IEEE T Power Electr* 36: 9237–9250. https://doi.org/10.1109/TPEL.2021.3052459
18. Hebala OM, Aboushady AA, Ahmed KH, Burgess S, Prabhu R (2018) Generalized Small-Signal Modelling of Dual Active Bridge DC/DC Converter. In *Proceedings of the 2018 7th International Conference on Renewable Energy Research and Applications (ICRERA)*, 914–919. https://doi.org/10.1109/ICRERA.2018.8567014
19. Gonzalez M, Cardenas V, Pazos F (2004) DQ Transformation Development for Single-Phase Systems to Compensate Harmonic Distortion and Reactive Power. In *Proceedings of the 9th IEEE International Power Electronics Congress*, 177–182. https://doi.org/10.1109/CIEP.2004.1437575
20. Bacha S, Munteanu I, Bratcu AI (2014) *Power Electronic Converters Modeling and Control: With Case Studies*, Advanced Textbooks in Control and Signal Processing, Springer-Verlag: London. https://doi.org/10.1007/978-1-4471-5478-5_1
21. Li L, Xu G, Sha D, Liu Y, Sun Y, Su M (2023) Review of Dual-Active-Bridge Converters with Topological Modifications. *IEEE T Power Electr* 38: 9046–9076. https://doi.org/10.1109/TPEL.2023.3258418
22. Campos-Salazar JM (2024) Design and Analysis of Battery Chargers for Electric Vehicles Based on Multilevel Neutral-Point- Lamped Technology. Doctoral thesis, Universitat Politècnica de Catalunya: Universitat Politècnica de Catalunya, 2024.
23. Campos Salazar J, Viani-Abad A, Sandoval-Garcá R (2024) Modeling and Simulation of a Single-Phase Linear Multi-Winding Transformer in the d-q Frame. *Journal of Electronics and Electrical Engineering* 3: 206–235. https://doi.org/10.37256/jeee.3120244530
24. Trento BC (2012) Modeling and Control of Single-Phase Grid-Tie Converters. Master's Theses.
25. Erickson RW, Maksimovic D (2013) *Fundamentals of Power Electronics*, Springer Science & Business Media.
26. Mohan N (2011) *Electric Machines and Drives: A First Course*, Hoboken, NJ.
27. Katsuhiko O (2009) *Modern Control Engineering*, Boston.
28. Kuo BC (1991) *Automatic Control Systems*, 6th edition., Prentice Hall: Englewood Cliffs, N.J.
29. Khalil H (2014) *Nonlinear Control*, 1st edition., Pearson: Boston.